A&A, 709, A168 (2026)
https://doi.org/10.1051/0004-6361/202658969

Astronomy & Astrophysics

Radiolysis versus photolysis of nitrile ices: Laboratory constraints for interstellar chemistry

Q. D. Borengasser*, B. M. Moore*, T. J. Hager, R. Johnson, K. T. Renshaw, and B. M. Broderick**

Department of Chemistry, University of Missouri, Columbia, Missouri 65211, USA

Received 15 January 2026 / Accepted 26 March 2026

ABSTRACT

Aims. Interstellar ice chemistry is a fundamental driver of the molecular complexity observed within the interstellar medium. Moreover, the chemical evolution of icy mantles is predominantly influenced by the energetic processes to which they are exposed. Differences between radiolytic and photolytic pathways for the formation of complex organic molecules (COMs) can lead to significant variations in the resulting molecular abundances.

Methods. Application of Chirped Pulse ICE enables the energetic processing of astrophysical ices through both vacuum ultraviolet photolysis and high-energy electron bombardment, facilitating direct comparison of the chemical outcomes produced by each radiation source. Within a single apparatus, ices are characterized in the condensed phase using reflection-absorption infrared spectroscopy, and in the gas phase directly following temperature-programmed desorption via chirped-pulse millimeter-wave rotational spectroscopy coupled with buffer gas cooling. Comparative energetic processing of two parent ices, methyl and ethyl cyanide (CH_3CN and CH_3CH_2CN), reveals several key findings.

Results. Following radiolysis, the formation of ketenimine (CH_2CNH) from methyl cyanide increases by a factor of 3.9–5.9 relative to hydrogen cyanide (HCN) production, compared to photolysis, with detection limited to the condensed phase. This enhancement increases to 7.0–8.3 for methyl ketenimine (CH_3CHCNH) formation from ethyl cyanide. In contrast, the abundance of the corresponding isonitrile relative to HCN remains consistent across both radiation sources, as evidenced by its detection in both the condensed and gas phase. Our results suggest that observed imine-to-HCN ratios may be diagnostic tracers of the prevailing energetic processing and chemical pathways to COM formation in specific interstellar environments.

Key words. ISM: abundances – cosmic rays – ISM: molecules

1. Introduction

Astrochemistry observations over the past several decades have revealed a rich molecular inventory within the interstellar medium (ISM), including a wide range of complex organic molecules (COMs) detected in both the gas phase and icy grain mantles (McGuire 2022). Recent infrared observations with the James Webb Space Telescope (JWST) provide unprecedented access to the composition of interstellar ices (McClure et al. 2023), complementing high-resolution gas phase measurements obtained with single-dish telescopes at facilities such as the Atacama Large Millimeter Array (ALMA) (Carpenter et al. 2022,) and, in the near future, the Next Generation Very Large Array (ngVLA) (Robert et al. 2018). Together, these capabilities highlight the importance of understanding how ice phase chemistry translates into observable gas phase molecular abundances.

In cold and dense regions of the ISM, molecules accrete efficiently onto submicron-sized dust grains, forming icy mantles in which chemical reactions proceed under the influence of energetic processing (Evans et al. 2012; Herbst 1995; Öberg 2016; Sagan 1972; Salpeter 1971). Ultraviolet (UV) photons and high-energy particles interact with these ices, generating radicals, ions, and secondary electrons that drive the formation of COMs. Laboratory experiments demonstrate that a wide variety of energetic sources often yield similar reaction products, while producing different relative abundances (Cuppen et al. 2024; Herrero et al. 2022; Hudson & Moore 2004; Muñoz Caro et al. 2014). Quantifying these differences is essential for connecting laboratory simulations with astronomical observations.

Comparative studies of photolysis and radiolysis show that particle irradiation can enhance bond cleavage and promote nonselective chemistry through cascades of low-energy secondary electrons (Arumainayagam et al. 2010; Förstel et al. 2015; Mason et al. 2014). However, most previous investigations rely on different experimental setups or detection techniques, complicating direct comparisons between irradiation sources. In addition, relatively few studies have systematically examined how condensed phase product distributions relate to gas phase abundances following sublimation, a connection that is critical for interpreting astronomical column densities.

Nitrogen-bearing COMs are particularly well suited for such investigations. Their large dipole moments make them favorable targets for radio astronomical observations, and many nitriles, isonitriles, and imines are widely detected in star-forming regions and hot cores (Johnson et al. 1977; Nazari et al. 2024a; Solomon et al. 1971). Despite their observational importance, the dominant formation pathways of these species, especially the role of photochemical versus particle-driven processes, remain uncertain. For example, previous studies found that varied energetic conditions yield enhancement of isomerization versus tautomerization pathways for N-COMs (Bulak et al. 2020; Hudson & Moore 2004; Mencos & Krim 2016). However, the exact efficiencies of different processes on the formation of these distinct products are poorly constrained due to lack of explicit relative product branching ratios.

* These authors equally contributed to this work.
** Corresponding author: broderickbm@missouri.edu

In this work, we addressed these questions through laboratory comparisons of vacuum ultraviolet (VUV) photolysis and high-energy electron irradiation of neat methyl cyanide (CH_3CN) and ethyl cyanide (CH_3CH_2CN) ices. By applying chirped-pulse ice (CPICE), we directly probed both condensed phase and gas phase reaction products via reflection-absorption infrared spectroscopy (RAIRS) and chirped-pulse millimeter-wave rotational spectroscopy (Brown et al. 2008), respectively. By quantifying product branching ratios under the same parent depletion conditions, we isolated the effects of irradiation sources on reaction pathways. Our results provide laboratory constraints on imine, nitrile, and isonitrile formation that are relevant to interpreting observations of nitrogen-bearing COMs in the ISM.

2. Materials and methods

This work was performed within CPICE, which has been previously described in detail (Hager et al. 2024; Radhakrishnan et al. 2022). Briefly, CPICE is a custom-built stainless-steel, ultra-high vacuum apparatus with a base pressure of 10^{-10} torr within which the radiation-induced chemistry of interstellar ice analogs is studied. Neat ices were generated through the deposition of CH_3CN or CH_3CH_2CN onto a 1 cm × 1 cm silver substrate held at 20 K. Ice thickness was determined by laser interferometry measurements with a 632.8 nm ThorLabs HeNe laser (Moore et al. 2010). The neat ices were energetically processed following irradiation by a Hamamatsu L10706 broadband VUV lamp, or, separately, with high-energy electrons by a Kimball Physics EGG-3101C electron gun. Ices were monitored before, during, and after irradiation by in situ RAIRS to observe parent depletion and new product growth. Following energetic processing, the 20 K ice rested for 1 hour prior to performing temperature-programmed desorption (TPD) at a ramping rate of 5 K/min. At the end of this rest period, the lower ice stage was raised to the 25 K buffer gas cell (BGC) into which the molecules entered upon reaching their sublimation temperature where they were promptly cooled through collisions with cold Ne atoms in the cell. The cooled molecules that possess a permanent dipole moment were then detected via chirped-pulse millimeter-wave spectroscopy from 65–90 GHz.

2.1. VUV photon processing

The VUV photolysis experiments discussed below have been described in detail (Hager et al. 2025); however, a summary is provided here to facilitate comparison with the present work. Neat CH_3CN or CH_3CH_2CN ices were deposited to achieve a thickness of approximately 1.6 microns and irradiated using a broadband VUV lamp to deliver a photon flux of $\sim 10^{15}$ photons cm^{-2} s^{-1}. The lamp output is dominated by emission at 160 nm (80%), with a 20% contribution from 120 nm, corresponding to an average incident photon energy of 8.26 eV. During irradiation, photon attenuation within the ice follows the Beer-Lambert law, which we applied here to estimate the photon penetration depth (Bulak et al. 2020):

$$I = I_o e^{-\sigma N_c}, \tag{1}$$

where I is the light intensity after passing through a given column density N_c, I_o is the incident light intensity, and σ is the photo absorption cross section. The column density is related to the thickness as

$$N_c = \frac{T \rho N_A}{m}, \tag{2}$$

where T is ice thickness, ρ is ice density, N_A is Avogadro's number, and m is the molar mass.

For the absorption cross section of condensed phase CH_3CN, we assumed the ice to gas phase ratio is the same as that for methanol, which is known (Bulak et al. 2020; Hager et al. 2025). This gives the condensed phase absorption cross section for CH_3CN as 7.5×10^{-18} cm^2. Equation (1) was then solved at several number densities to get the light intensity after passing through the ice.

The ratio of I:I_o gives the percentage of photons which pass through a given ice thickness. We find that 99% of photons are retained in the ice within a depth of 0.5 microns for CH_3CN. Furthermore, the average penetration depth of a photon in each ice was determined to be ~0.11 microns, well below the total ice thickness used in this work. In these experiments, ices were exposed to VUV irradiation for 3 hours, with a resulting fluence of 1.1×10^{19} photons cm^{-2}. Considering the expected photon flux imposed on an icy mantle in a dense molecular cloud from Cecchi-Pestellini & Aiello (1992) of $\sim 10^4$ photons cm^{-2} s^{-1}, our resultant interstellar timescale is ~35 Myr, which is not unreasonable considering the evolution lifetimes of these clouds (Chevance et al. 2019). During the irradiation procedure, parent depletion was monitored via RAIRS. This resulted in a parent depletion of 12% for CH_3CN and 20% for CH_3CH_2CN. Using the corresponding difference in the number of parent molecules destroyed, an absorption cross section for CH_3CH_2CN was found to be 8.31×10^{-18} cm^2. This results in an average penetration depth of ~0.15 microns and a characteristic thickness for 99% photon retention of 0.7 microns for CH_3CH_2CN experiments. Energetically, this can be described by a calculated dosage (eV $molec^{-1}$ s^{-1}):

$$D_s = \frac{P_c E_{\text{photon}} m}{N_A \rho A l}. \tag{3}$$

In Eq. (3), P_c is the photon current of the lamp, E_{photon} is the average photon energy, A is the irradiated area, and l is the average photon penetration depth. For CH_3CN this equates to 6.5×10^{-2} eV $molec^{-1}$ s^{-1} and for CH_3CH_2CN it is 7.1×10^{-2} eV $molec^{-1}$ s^{-1}.

2.2. 5 keV electron processing

A second radiation source of high-energy electrons was employed to compare with the results observed in our VUV photolysis. Neat CH_3CN or CH_3CH_2CN ices approximately 1 micron thick were irradiated with a 5 keV electron beam operated at 30 nA at an incident angle of 16.5°. The electron spot size was ~3 mm in diameter. The interaction of electrons with the condensed phase samples was characterized using Monte Carlo simulations performed with Casino 2.5 (Hovington et al. 1997). Simulations of 5×10^6 electrons provided the depth-dependent energy deposition profiles necessary for calculating the irradiation dosage, as described by Förstel et al. (2015):

$$D_s = \frac{lm}{eN_A \rho A l}(E_{\text{int}} - f_{\text{trans}} E_{\text{trans}} - f_{bs} E_{bs}), \tag{4}$$

where I is the electron irradiation current, e is the fundamental charge of an electron, and E_{int} is the energy of incident electrons. The series of f_x variables describes the fraction of electrons that may interact with the ice in some way (transmitted through the ice and backscattered from the ice surface), with the associated E_x representing the average energy of this fraction of electrons. Given the conditions employed in this work,

the dosage for the CH_3CN ice was 1.4×10^{-3} eV molec^{-1} s^{-1} and 1.9×10^{-3} eV molec^{-1} s^{-1} for CH_3CH_2CN. At these dosages, CH_3CN was irradiated for 40 min to achieve a 12% parent depletion, while CH_3CH_2CN was irradiated for 50 min to achieve a parent depletion of 20%, consistent with that observed in the VUV experiments described above. Considering an electron flux in a dense molecular cloud to be $\sim 10^2$ cm^{-2} s^{-1} and the average energy of the electrons initiating ice grain chemistry to be 10–20 eV (Wu et al. 2024), the lifetime to achieve a dosage similar to that used in our experiment is ~5 Myr.

2.3. Irradiation source comparison

The irradiation procedures described above yielded a comparable overall parent molecule destruction in the neat ices. However, the penetration depth of radiation differs substantially between the two sources (Öberg 2016). Vacuum ultraviolet photons were absorbed predominantly within the upper ~100 nm of the ice, calculated by Beer's Law, whereas 5 keV electrons penetrated more deeply, via Monte Carlo simulations, resulting in a larger effective irradiated volume. This disparity is reflected in the calculated dosage rates, which are $\sim 10^{-2}$ eV molec^{-1} s^{-1} for photons and 10^{-3} eV molec^{-1} s^{-1} for electrons. Furthermore, the effective interstellar lifetimes for each experiment vary significantly. Although these differences will influence the total abundance of products formed in either case, meaningful relative abundances within each experiment allow comparison between the two irradiation sources. The different chemical outcomes observed under electron and VUV irradiation can be attributed to the distinct energy distributions of the reactive species they generate. Electron irradiation produces a broad cascade of secondary electrons, with a substantial fraction retaining energies in the ~10–20 eV range (Arumainayagam et al. 2019), whereas VUV irradiation generates photoelectrons and excitations at energies below the MgF_2 cutoff of ~10.8 eV. As a result, electron-driven processing accesses a wider range of inelastic collision channels, including ionization and higher-energy dissociation pathways that are energetically inaccessible under Lyman-α (Ly-α) and longer wavelength irradiation. The higher-energy electrons arising from electron-irradiated ices in turn lead to more extensive chemical processing and access to reaction channels with higher energy barriers.

2.4. RAIRS in situ detection

Ices were monitored in situ before, during, and after energetic processing via RAIRS to determine both parent-molecule depletion and product branching ratios. Column densities were calculated following the procedure outlined by Hudson & Moore (2004), using infrared band strengths for species with well-characterized absorption features:

$$N_c = \frac{\int \tau(\nu) \mathrm{d}\nu}{A}. \quad (5)$$

Here, the column density (N_c) is equal to the integration of the band intensity across frequency ($\tau(\nu)\mathrm{d}\nu$) of the band of interest divided by the assumed band strength (A) for that vibrational mode. Because infrared bands may not be uniquely attributable to a single molecular species, each assignment must satisfy established validation criteria (Öberg et al. 2009). Table 1 gives the detected species and the bands used to quantify them.

To the best of our knowledge, no infrared band strengths have been reported for the iso-species (CH_3NC and CH_3CH_2NC) observed in this work. Previous studies have assumed that the NC stretching modes of these isomers could be approximated using the band strengths of the corresponding CN stretches of their nitrile counterparts (Hudson & Moore 2004; Carvalho & Pilling 2020), despite knowledge that this was likely an underestimation of the -NC band strength (Couturier-Tamburelli et al. 2018). Product branching ratios obtained following VUV photolysis indicate that the -NC and -CN band strengths differ and have been constrained through comparison of the condensed phase and gas phase measurements afforded by CPICE (Hager et al. 2025). Additional experiments confirming these differences will be described in a forthcoming manuscript.

Table 1. Vibrational frequencies and assumed band strengths used for solid-phase column densities.

Species	Frequency (cm^{-1})	A (cm molec^{-1})	Integration (cm^{-1})
CH_3CN^*	2251; CN st.	2.2×10^{-18}(1,2)	2267–2231
$CH_3CH_2CN^*$	2245; CN st.	2.8×10^{-18}(3,4)	2279–2232
CH_2CHCN^b	2227; CN st.	4.0×10^{-18}(5)	2231–2216
CH_3NC^a	2168; NC st.	8.4×10^{-18}(6)	2181–2157
$CH_3CH_2NC^b$	2155; NC st.	8.4×10^{-18}(6)	2165–2145
$HCN^{a,b}$	2083; CN st.	1.1×10^{-17}(3)	2100–2071
CH_2CNH^a	2034; CCN st.	7.2×10^{-17}(1)	2070–1990
CH_3CHCNH^b	2034; CCN st.	7.2×10^{-17}(1)	2068–1980
CH_4^a	1305; CH def.	9.7×10^{-18}(7)	1319–1288

Notes. * Species marked with an asterisk are the parent ices. a Species formed following energetic processing of CH_3CN. b Species formed following energetic processing of CH_3CH_2CN. (1) Hudson & Moore (2004); (2) Rachid et al. (2022); (3) Gerakines et al. (2021); (4) Moore et al. (2010); (5) Toumi et al. (2016); (6) Hager et al. (2025); (7) Gerakines & Hudson (2015).

2.5. Broadband millimeter-wave gas phase detection

For the gas phase product branching ratio analysis of the processed ices, millimeter-wave rotational spectroscopy was employed. Desorption into the gas phase was achieved via TPD at a heating rate of 5 K/min. The desorbed molecules entered the BGC, where collisions with Ne promptly cooled them to a rotational temperature of ~25 K, enabling sensitive detection by chirped-pulse rotational spectroscopy. The relative abundances of the gas phase products in each experiment were then quantified using Eq. (6) (Borengasser et al. 2023; Dias et al. 2018; Endres et al. 2016; Gordy & Cook 1984):

$$N = \frac{IQ(T)}{\nu S \mu^2 g \left(e^{\frac{-E''}{kT}} - e^{\frac{-E'}{kT}}\right)}. \quad (6)$$

The number density (N) of each detected species was used to compare their relative abundances. The measured signal intensity (I) was corrected for several spectroscopic factors, including the rotational partition function ($Q(T)$), transition frequency (ν), line strength (S), and square of the dipole moment (μ). A Boltzmann factor accounting for the energies of the upper (E') and lower (E'') rotational states was also applied. Table 2 summarizes the transitions used to quantify the gas phase products analyzed in this work. It should be noted that we resolved the hyperfine peaks for the HCN J = 1-0 transition caused by the ^{14}N nucleus present in the molecule.

Table 2. Rotational transitions used to quantify irradiation products in the gas phase.

Species	Frequency (GHz)	Transition	$S\mu^2$
CH_3CH_2CN[a]	79.6775	$9_{0,9}-8_{0,8}$	133.15
CH_3NC[a]	80.4219	4_0-3_0	121.07
CH_2CHCN[b]	87.3128	$9_{1,8}-8_{1,7}$	388.11
CH_3CH_2NC[b]	88.0743	$9_{2,7}-8_{2,6}$	122.88
CH_3CH_2CN[a]	88.3237	$10_{0,10}-9_{0,9}$	147.88
HCN[a,b]	88.6313	$1-0^*$	26.74

Notes. a Species formed following energetic processing of CH_3CN. b Species formed following energetic processing of CH_3CH_2CN. * Seen as hyperfine split peaks for f 1-1, 2-1, and 0-1.

3. Results

3.1. Methyl cyanide parent

Following both VUV photon processing and high-energy electron irradiation of the CH_3CN parent ices, the same set of products were detected by RAIRS, as illustrated in Fig. 1. These include the structural isomer of the parent species, methyl isocyanide (CH_3NC), hydrogen cyanide (HCN), the tautomer of the parent, ketenimine (CH_2CNH), and methane (CH_4). We previously reported a feature at 1130 cm^{-1} attributed to methylamine (CH_3NH_2) (Hager et al. 2025), consistent with the assignments suggested in Carvalho & Pilling (2020). However, our reassessment indicates that this feature cannot be unambiguously assigned to CH_3NH_2. Hudson & Moore (2004) noted that a band in this region may instead arise from CH_2CNH, whose presence in our experiments was independently confirmed by the CCN st. at 2034 cm^{-1}. Computational work by Tschöpe et al. (2021) places the ν_5 band for CH_2CNH at 1140 cm^{-1}, and experimental studies report this feature at 1127 and 1124 cm^{-1} (Bane et al. 2011; Jacox & Milligan 1963; Jacox 1979). In combination with the relatively weak band strength of the CH_3NH_2 mode (Rachid et al. 2021), these data indicate that the two species cannot be distinguished on the basis of this infrared feature alone.

The ices were subsequently warmed via TPD at a rate of 5 K/min, and the desorbed species were detected in the gas phase by chirped-pulse millimeter-wave rotational spectroscopy. As shown in Fig. 2, the same set of molecules was observed for both irradiation techniques. Gas phase detection enables the identification of CH_3CH_2CN, a product that cannot be distinguished in the condensed phase due to the overlap of its infrared features with those of the CH_3CN parent. Additional gas phase products observed include CH_3NC and HCN. CH_4 was not observed due to its lack of a permanent electric dipole moment, and CH_2CNH remains below our detection limit as its available rotational transitions have unfavorable intensities at 25 K within this spectral window. Notably, the two irradiation procedures give rise to distinct desorption profiles; a discussion of this behavior is provided in Sect. 4.3.

Condensed and gas phase branching ratios were then compared between the two irradiation sources, as shown in Table 3. All species were normalized to HCN, which was observed in both phases for both parents. Agreement between condensed and gas phase abundances was observed, suggesting thermal stability of the resulting products during warm-up. The relative abundance of CH_3NC in each source is similar. However, there are clear differences in the production of CH_3CH_2CN, which was greatly depleted in the electron-irradiated ice, and CH_2CNH, which was preferentially formed via electron irradiation.

3.2. Ethyl cyanide parent

The products formed from irradiation of CH_3CH_2CN ice were analyzed in the same fashion, as described above. Both irradiation sources generated the same suite of products, including acrylonitrile (CH_2CHCN), the structural isomer of the parent, ethyl isocyanide (CH_3CH_2NC), HCN, and methyl ketenimine (CH_3CHCNH), as shown in Fig. 3.

In contrast to the CH_3CN system, these products all possess permanent dipole moments and are therefore, in principle, detectable in the gas phase, as shown in Fig. 4. To our knowledge, the rotational spectrum of CH_3CHCNH is unknown, and its assignment is outside of the scope of this work. It was therefore not detected in the gas phase following TPD in these experiments. In addition, CH_3CH_2NC could not be quantified in the gas phase following electron irradiation due to its reduced abundance relative to photolysis experiments. To verify its formation, an additional experiment incorporating a third layer of processed CH_3CH_2CN ice was performed. Associated experimental data can be found in the appendix.

Product branching ratios were again determined in both the condensed and gas phase and subsequently compared in Table 4. Relative to HCN, the tautomer of the parent, CH_3CHCNH, was again significantly enhanced following electron irradiation. In addition, CH_2CHCN exhibited an increased relative abundance in the electron-processed ices. The extent of isomerization, however, remains comparable between the two irradiation methods.

4. Discussion

4.1. Irradiation effects

Although VUV photolysis and high-energy electron irradiation produced the same set of reaction products in both CH_3CN and CH_3CH_2CN ices, our results indicate that the relative efficiencies of the reaction pathways involved depend upon the irradiation source. This finding is consistent with previous laboratory studies showing that different energetic sources yield similar products with distinct branching ratios (Hudson & Moore 2004; Martín-Doménech et al. 2024). In particular, electron irradiation lead to enhanced formation of imines, relative to HCN, in comparison with VUV photolysis. This behavior reflects fundamental differences in how energy is deposited within the ice. Vacuum ultraviolet photons primarily induce localized photochemical processes, including selective bond cleavage or photoisomerization (Arumainayagam et al. 2019). In contrast, energetic electrons generate cascades of low-energy secondary electrons from a single incident particle, driving nonselective chemistry and a broad distribution of reactive intermediates within a small volume of the ice (Arumainayagam et al. 2010, 2019; Mullikin et al. 2019). These conditions favor nonselective reactions and radical-radical recombination pathways, increasing the probability of hydrogen rearrangement processes required for imine formation. The similar relative efficiencies of nitrile-to-isonitrile isomerization under both irradiation sources suggest that this pathway is comparatively insensitive to the detailed nature of energy deposition, in contrast to imine production. Moreover, despite unknown VUV absorption cross sections, this comparative approach remains valid, revealing the mechanistic contrasts between photolysis and radiolysis and their distinct astrochemical implications.

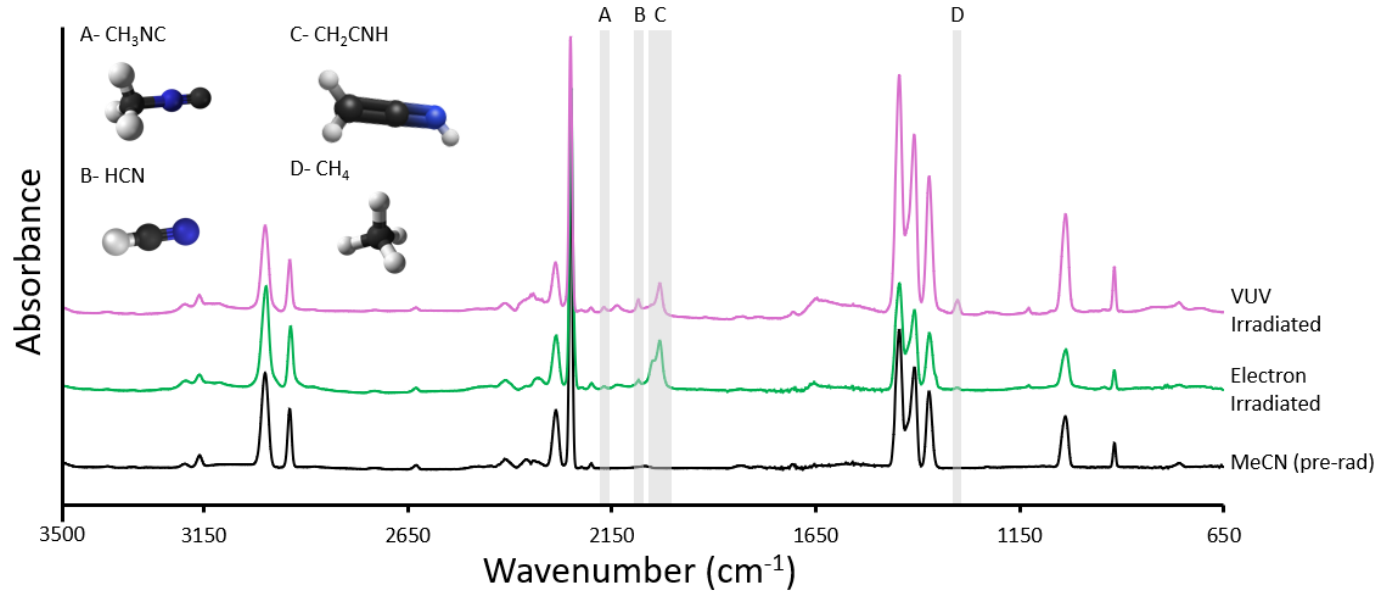

Fig. 1. RAIRS of CH_3CN before irradiation (black), post electron irradiation (green), and post VUV photon processing (pink). Products are highlighted and labeled with the structure inset in the top left.

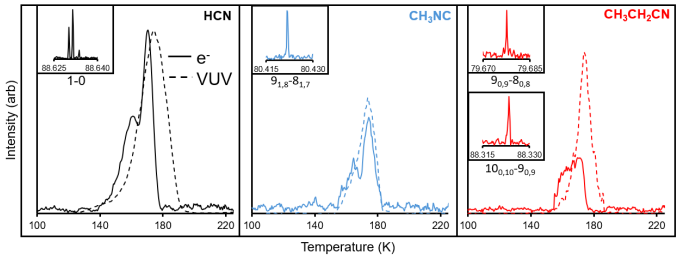

Fig. 2. TPD profiles of the gas phase products from CH_3CN parent ice irradiation and corresponding millimeter-wave spectrum inset. In the TPD profile, the solid lines indicate the electron-irradiated products, and the dashed lines indicate photolysis products.

Table 3. Product branching ratios for each irradiation source in both the condensed and gas phase for the CH_3CN parent.

CH_3CN	Condensed phase		Gas phase	
Species	VUV	Electrons	VUV	Electrons
HCN	1	1	1	1
CH_3NC	0.6 (0.1)	0.7 (0.1)	0.8 (0.1)	0.5 (0.1)
CH_3CH_2CN	OL	OL	1.0 (0.1)	0.3 (0.0)
CH_2CNCH	0.9 (0.1)	4.0 (0.4)	LOD	LOD
CH_4	1.7 (0.4)	1.0 (0.2)	ND	ND

Notes. OL – Overlap of band in the RAIRS spectrum. LOD – Outside the limit of detection based on transition strength and number of molecules formed. ND – No permanent dipole moment preventing millimeter-wave detection.

4.2. Imine production

An important finding in this work was the enhanced production of imines (relative to HCN) under electron irradiation for both parent molecules investigated. For CH_3CN, CH_2CNH formation increased by a factor of ~3.9–5.9 relative to photolysis, while for CH_3CH_2CN, CH_3CHCNH formation was enhanced by a factor of ~7.0–8.3. These trends, illustrated in Fig. 5, show product formation rates as a function of parent ice destruction under both irradiation types. Similar trends have been qualitatively reported in earlier work comparing particle irradiation and photolysis of nitrile-containing ices (Bulak et al. 2021; Mencos & Krim 2016). For example, Hudson & Moore (2004) compared UV photolysis with 0.8 MeV proton irradiation of CH_3CN ices and, although they did not report absolute abundances, found that proton irradiation substantially enhances the formation of CH_2CNH relative to the corresponding isocyanide. This enhancement was not observed in the photolysis experiments. The present study provides a direct, quantitative comparison of these species formed following energetic processing by electrons and photons. The preferential formation of imines under radiolytic processing clearly reflects the increased energy available from the secondary electron cascades, which facilitate higher-energy rearrangements required to form imines (Arumainayagam et al. 2019; Danger et al. 2011). This interpretation is consistent with the homolytic, roaming-like mechanism proposed Wentrup et al. (2017), in which tautomerization of CH_3CN to CH_2CNH proceeds over a barrier of 4 eV. This barrier is comparable to those inferred from laser ablation experiments and lower-level density functional theory calculations from Cho (2013). In contrast, the isomerization barrier from CH_3CN to CH_3NC is found to be lower by 1.11 eV, suggesting that this pathway is more readily accessed under UV photolysis, where the available energy is more limited. Deuterium labeling experiments (Hudson & Moore 2004) suggested imine formation is an intramolecular process, so there is no need to invoke intermolecular chemistry.

While the detailed microscopic mechanisms remain uncertain, the reproducibility of this enhancement of imine formation across two chemically related parent species suggests it is a general feature of radiolytically processed nitrile ices. From an astrochemical perspective, this result implies that imine-to-nitrile abundance ratios may be sensitive to the dominant energetic processing mechanism in a given environment. Regions where particle-driven chemistry plays a larger role, such as dense molecular cloud interiors shielded from external UV radiation, may preferentially produce higher imine

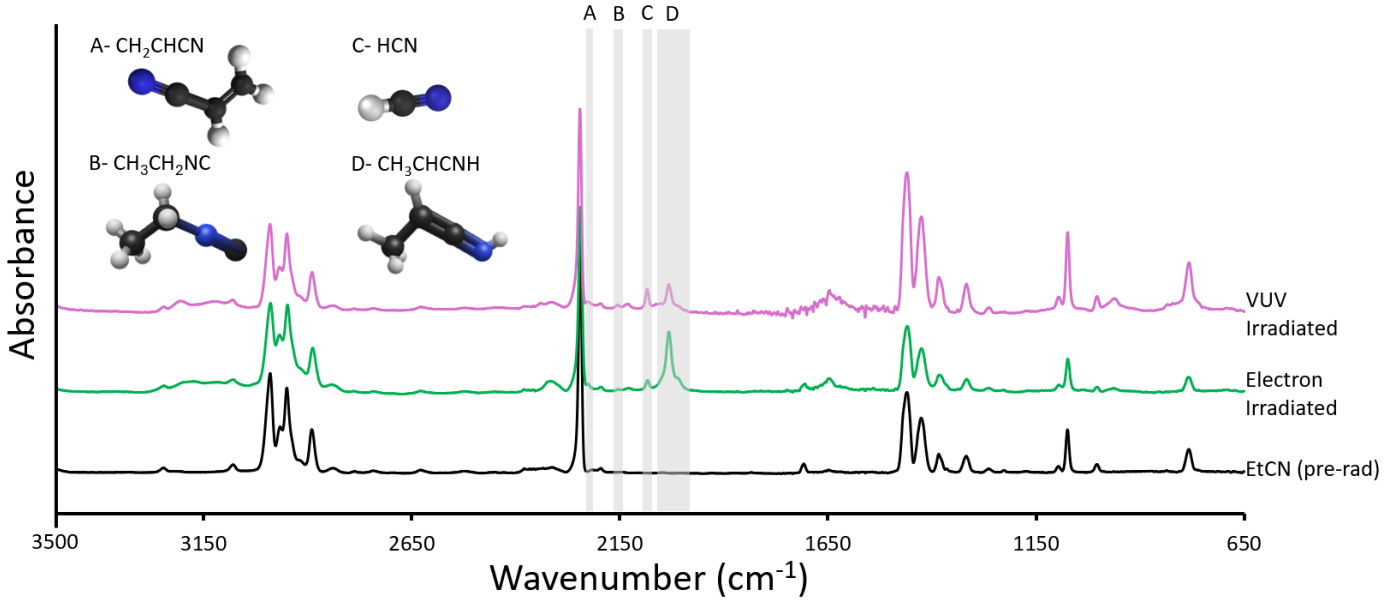

Fig. 3. RAIRS of the CH_3CH_2CN parent ice before irradiation (black), post electron irradiation (green), and post VUV photon processing (pink). Products are highlighted and labeled with the structure inset in the top left.

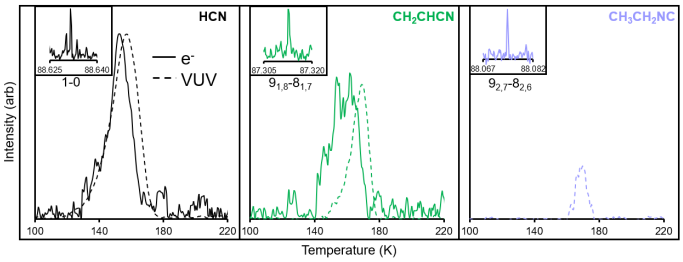

Fig. 4. TPD profiles of the gas phase products from the CH_3CH_2CN parent ice irradiation and corresponding millimeter-wave spectrum inset. In the TPD profile, the solid lines indicate electron-irradiated products, and the dashed lines indicate photolysis products.

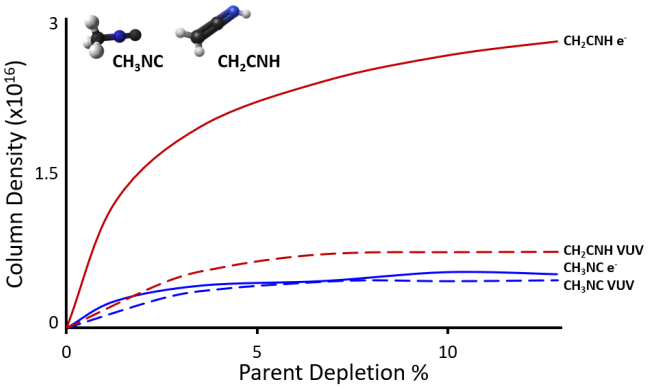

Fig. 5. Product formation monitored during irradiation via RAIRS. The red lines show the CH_2CNH product, and the blue lines show the CH_3NC product. The solid line indicates electron irradiation, and the dashed line indicates VUV photolysis.

Table 4. Product branching ratios for each irradiation source in both the condensed and gas phase for the CH_3CH_2CN parent.

CH_3CH_2CN	Condensed phase		Gas phase	
Species	VUV	Electrons	VUV	Electrons
HCN	1	1	1	1
CH_3CH_2NC	0.2 (0.0)	0.2 (0.0)	0.2 (0.0)	LOD
CH_2CHCN	0.5 (0.1)	0.7 (0.0)	0.4 (0.1)	0.8 (0.2)
CH_3CHCNH	0.3 (0.0)	2.4 (0.1)	US	US

Notes. LOD – Outside the limit of detection based on transition strength and number of molecules formed. US – Unknown spectrum for millimeter-wave detection.

abundances relative to nitriles than regions dominated by photochemistry.

4.3. Ice composition and morphology

The two irradiation methods produce distinct desorption profiles, most notably for the CH_3CN parent ice. In all experiments, products formed via VUV photolysis desorb at slightly higher temperatures than those produced by electron irradiation, with TPD peak maxima shifted by 2–5 K. For CH_3CN-derived products, desorption begins ~140 K for HCN and ~155 K for CH_3CH_2CN and CH_3NC under both irradiation conditions. However, VUV-processed ices exhibited smooth, monotonic TPD profiles, whereas electron-irradiated samples display two distinct features within the desorption curves. These features occur at ~162 K for HCN and ~168 K for CH_3NC, ~12 K beyond the onset of desorption, and were absent in the CH_3CH_2CN experiments. Such differences are indicative of irradiation-dependent modifications to ice structure and composition. This interpretation is consistent with previous studies demonstrating that ice morphology strongly influences TPD behavior and that energetic processing can substantially alter desorption kinetics (Ayling et al. 2017; Bolina et al. 2005; Borengasser et al. 2023; Green et al. 2009). Energetic processing is known to induce amorphization in molecular ices, with both UV photons and electrons capable of disrupting crystalline order at low temperatures

(Kouchi & Kuroda 1990; Lepault et al. 1983). In addition, amorphous ices have been shown to undergo more efficient destruction and product formation under electron irradiation than their crystalline counterparts (Mifsud et al. 2022).

In this work, the contrasting desorption behavior observed following VUV photolysis and electron bombardment suggests different degrees of ice homogeneity. Electron irradiation deposits energy over a larger depth than VUV photons, which are absorbed primarily in the near-surface layers, leading to more extensive structural disruption and the redistribution of reaction products throughout the bulk. These differences in energy-deposition profiles likely give rise to distinct ice morphologies and in turn different desorption characteristics, making parent-parent interaction effects more relevant under radiolysis than photolysis conditions. Previous studies of CH_3CN and CH_3CH_2CN ices further highlight the sensitivity of these systems to deposition and thermal history (Smith et al. 2021; Hudson 2020), highlighting the importance of ice morphology in interpreting the results presented here.

4.4. Astrophysical implications

Establishing a clear distinction between radiolysis- and photolysis-driven reactions in astrophysical environments remains challenging, as both processes occur simultaneously and promote similar chemistry in ices. In dense molecular clouds, external UV radiation is strongly attenuated. Instead, energetic processing is driven predominantly by the Prasad-Tarafdar mechanism, in which cosmic-ray induced secondary electrons excite molecular hydrogen, whose radiative relaxation produces a field dominated by Ly-α UV photons (Arumainayagam et al. 2019; Gredel et al. 1989; Prasad & Tarafdar 1983). These same cosmic-ray generated secondary electrons are also the primary way in which chemistry in ices occurs, leading to parallel photochemical and electron-driven pathways within the same environment. Under these conditions, isolating the dominant mechanism responsible for molecular complexity in dense clouds is difficult. Nevertheless, laboratory comparisons of photolysis and radiolysis, such as those presented here, provide important constraints on the relative efficiencies and product branching ratios associated with each process. These constraints can inform the interpretations of astronomical column densities, guide searches for new molecules, and help characterize variations in local physical conditions across the ISM. In particular, the distinct relative abundances of imines and isonitriles observed in this work offer a potential diagnostic for evaluating the relative impact between photochemical and radiolytic processing in astrophysical ices. Assuming a radiolytically enhanced region with an approximate 75:25 radiolysis-to-photolysis contribution, our results predict abundance ratios of ~3.2:1 for CH_2CNH:HCN and ~1.9:1 for CH_3CHCNH:HCN. Detection of such ratios would be indicative of UV shielding or elevated comic-ray fluxes. Other factors, such as increased ice temperatures that enhance H-atom mobility, or more complex ice compositions, may also influence these ratios. While additional experiments will be performed to explore these effects, the present results demonstrate the sensitivity of N-COMs to the dominant energy source.

Although the present experiments focus on water-free ices, such simplified compositions are astrophysically relevant and isolate intrinsic chemical pathways. This work provides direct constraints on energetic processing in nonaqueous environments, such as Titan's atmosphere and surface, where oxygen-bearing species are scarce and N and hydrocarbon species dominate (Lv et al. 2017). Under these conditions, chemistry is driven primarily by energetic electrons and photons rather than aqueous or hydrogen-bonded networks. Laboratory investigations of water-poor ices therefore complement the studies of H_2O-rich interstellar mantles by disentangling matrix effects from fundamental reaction mechanisms.

Beyond constraining formation pathways, the application of CPICE enables direct comparison of product abundances in the condensed phase and those observed following sublimation into the gas phase under controlled laboratory conditions. Recent observational advances with JWST now permit analogous comparisons in astrophysical environments, providing an essential context for interpreting laboratory results. The JWST Observations of Young protoStars (JOYS) program (van Dishoeck et al. 2025) targets protostellar sources spanning a range of masses and luminosities, providing unprecedented insight into the chemical connection between icy grain mantles and the gas phase. Combined JWST and ALMA studies have demonstrated that ice and gas phase abundance ratios for certain cyanides, such as CH_3CH_2CN/CH_3CN, are broadly consistent across multiple sources (Nazari et al. 2022, 2024a), suggesting similar formation pathways and efficient inheritance from the ice to the gas phase.

In contrast, abundance ratios of N-COMs relative to CH_3OH often differ by factors of 5 to ~20 (Nazari et al. 2024a). These discrepancies are in part attributed to physical effects associated with differing sublimation temperatures, binding energies, and snowline locations rather than fundamental chemical differences. Nazari et al. (2021) demonstrated that variations in desorption temperatures can produce apparent gas phase column density ratio scatter that does not reflect true ice abundances. However, applying correction factors based upon relative sublimation temperatures significantly improves gas-ice agreement. Subsequent radiative transfer modeling reproduced observed abundance scatter across ~40 protostellar systems, showing reduced variance for species with similar desorption temperatures (Nazari et al. 2024b).

Recent JWST-ALMA comparisons of oxygen-bearing COMs (Chen et al. 2024) further support this interpretation, with comparable gas and ice phase ratios observed for species such as CH_3OCHO and CH_3OCH_3 relative to CH_3OH, consistent with direct inheritance or strong chemical coupling. The similarly consistent gas-ice ratios observed for the N-COMs studied here indicate that physical effects during sublimation are limited and that relative abundances are largely preserved during the ice-to-gas transition.

These results highlight the need for continued laboratory investigations that bridge the gap between experimental astrophysics and observational astronomy. Experiments that vary energy sources under controlled conditions, while simultaneously probing condensed and gas phase products, provide meaningful abundance baselines for comparison with JWST and radio telescopes. Such integrated approaches will be essential for refining our understanding of the chemical evolution of interstellar environments.

5. Conclusions

Following VUV photolysis or 5 keV electron irradiation of neat CH_3CN or CH_3CH_2CN ice, we observe formation of the same products, but with distinct relative abundances through a combination of in situ condensed phase detection via RAIRS and broadband millimeter-wave spectroscopy for gas phase detection. For both parent molecules, electron irradiation produces a higher yield of the imine species relative to HCN, suggesting

that radiolytic energy deposition may facilitate parent-fragment interactions or tautomerization pathways more efficiently than VUV photolysis. However, neither processing method appears to preferentially promote parent isomerization, and the agreement between condensed phase and gas phase branching ratios suggest that the detected products are thermally stable during warm-up. In addition to differences in product abundances between species, we also observe distinct desorption behaviors for the CH_3CN system between electron and photon processing. Future experiments aimed at clarifying the origins of these differences in desorption behavior will be performed.

Data availability

The data generated in this study are available upon request.

Acknowledgements. We gratefully acknowledge the National Science Foundation Advanced Manufacturing Program, Grant No. 2314347, and The Cottrell Scholar Award No. CS-CSA-2024-016 from the Research Corporation for Science Advancement.

References

Arumainayagam, C. R., Lee, H.-L., Nelson, R. B., Haines, D. R., & Gunawardane, R. P. 2010, Surf. Sci. Rep., 65, 1
Arumainayagam, C. R., Garrod, R. T., Boyer, M. C., et al. 2019, Chem. Soc. Rev., 48, 2293
Ayling, S. A., Burke, D. J., Salter, T., & Brown, W. A. 2017, RSC Adv., 7, 51621
Bane, M. K., Thompson, C. D., Robertson, E. G., Appadoo, D. R. T., & McNaughton, D. 2011, PCCP, 13, 6793
Bolina, A. S., Wolff, A. J., & Brown, W. A. 2005, JPC B, 109, 16836
Borengasser, Q., Hager, T., Kanaherarachchi, A., Troya, D., & Broderick, B. M. 2023, JPCL, 14, 6550
Brown, G. G., Dian, B. C., Douglass, K. O., et al. 2008, Rev. Sci. Instrum., 79, 053103
Bulak, M., Paardekooper, D. M., Fedoseev, G., & Linnartz, H. 2020, A&A, 636, A32
Bulak, M., Paardekooper, D. M., Fedoseev, G., & Linnartz, H. 2021, A&A, 647, A82
Carpenter, J., Brogan, C., Iono, D., & Mroczkowski, T. 2022, arXiv e-prints [arXiv:2211.00195]
Carvalho, G. A., & Pilling, S. 2020, JPC A, 124, 8574
Cecchi-Pestellini, C., & Aiello, S. 1992, MNRAS, 258, 125
Chen, Y., Rocha, W. R. M., van Dishoeck, E. F., et al. 2024, A&A, 690, A205
Chevance, M., Kruijssen, J. M. D., Hygate, A. P. S., et al. 2019, MNRAS, 493, 2872
Cho, H.-G. 2013, BKCS, 34, 1361
Couturier-Tamburelli, I., Toumi, A., Piétri, N., & Chiavassa, T. 2018, Icarus, 300, 477
Cuppen, H. M., Linnartz, H., & Ioppolo, S. 2024, ARA&A, 62, 243
Danger, G., Bossa, J. B., de Marcellus, P., et al. 2011, A&A, 525, A30
Dias, N., Joalland, B., Ariyasingha, N. M., Suits, A. G., & Broderick, B. M. 2018, JPC A, 122, 7523
Endres, C. P., Schlemmer, S., Schilke, P., Stutzki, J., & Müller, H. S. P. 2016, J. Mol. Spectrosc., 327, 95
Evans, A. C., Meinert, C., Giri, C., Goesmann, F., & Meierhenrich, U. J. 2012, Chem. Soc. Rev., 41, 5447
Förstel, M., Maksyutenko, P., Jones, B. M., et al. 2015, ChemPhysChem, 16, 3139
Gerakines, P. A., & Hudson, R. L. 2015, ApJ, 805, L20
Gerakines, P. A., Yarnall, Y. Y., & Hudson, R. L. 2021, MNRAS, 509, 3515
Gordy, W., & Cook, R. L. 1984, Microwave Molecular Spectra, 3rd edn. (New York: Wiley), 18
Gredel, R., Lepp, S., Dalgarno, A., & Herbst, E. 1989, IAU Colloq., 120, 32
Green, S. D., Bolina, A. S., Chen, R., et al. 2009, MNRAS, 398, 357
Hager, T. J., Moore, B. M., Borengasser, Q. D., et al. 2024, JCP, 161, 094201
Hager, T. J., Moore, B. M., Borengasser, Q. D., et al. 2025, ACS Earth Space Chem., 9, 2137
Herbst, E. 1995, Annu. Rev. Phys. Chem., 46, 27
Herrero, V. J., Tanarro, I., Jiménez-Serra, I., et al. 2022, MNRAS, 517, 1058
Hovington, P., Drouin, D., & Gauvin, R. 1997, Scanning, 19, 1
Hudson, R. L. 2020, Icarus, 338, 113548
Hudson, R. L., & Moore, M. H. 2004, Icarus, 172, 466
Jacox, M. E. 1979, Chem. Phys., 43, 157
Jacox, E., & Milligan, D. E. 1963, JACS, 85, 278
Johnson, D. R., Lovas, F. J., Gottlieb, C. A., et al. 1977, ApJ, 218, 370
Kouchi, A., & Kuroda, T. 1990, Nature, 344, 134
Lepault, J., Freeman, R., & Dubochet, J. 1983, J. Microsc., 132, RP3
Lv, K.-P., Norman, L., & Li, Y.-L. 2017, Astrobiology, 17, 1173
Martín-Doménech, R., Öberg, K. I., Muñoz Caro, G. M., et al. 2024, MNRAS, 535, 807
Mason, N. J., Nair, B., Jheeta, S., & Szymańska, E. 2014, Faraday Discuss., 168, 235
McClure, M. K., Rocha, W. R. M., Pontoppidan, K. M., et al. 2023, Nat. Astron., 7, 431
McGuire, B. A. 2022, ApJS, 259, 30
Mencos, A., & Krim, L. 2016, MNRAS, 460, 1990
Mifsud, D. V., Hailey, P. A., Herczku, P., et al. 2022, PCCP, 24, 10974
Moore, M. H., Ferrante, R. F., James Moore, W., & Hudson, R. 2010, ApJS, 191, 96
Mullikin, E., Hay, A., Anderson, H., O'Hern, N., & Arumainayagam, C. 2019, Proc. IAU, 15, 361
Muñoz Caro, G. M., Dartois, E., Boduch, P., et al. 2014, A&A, 566, A93
Nazari, P., van Gelder, M. L., van Dishoeck, E. F., et al. 2021, A&A, 650, A150
Nazari, P., Meijerhof, J. D., van Gelder, M. L., et al. 2022, A&A, 668, A109
Nazari, P., Rocha, W. R. M., Rubinstein, A. E., et al. 2024a, A&A, 686, A71
Nazari, P., Tabone, B., Rosotti, G. P., & van Dishoeck, E. F. 2024b, A&A, 687, A263
Öberg, K. I. 2016, Chem. Rev., 116, 9631
Öberg, K. I., Garrod, R. T., van Dishoeck, E. F., & Linnartz, H. 2009, A&A, 504, 891
Prasad, S. S., & Tarafdar, S. P. 1983, ApJ, 267, 603
Rachid, M. G., Brunken, N., de Boe, D., et al. 2021, A&A, 653, A116
Rachid, M. G., Rocha, W. R. M., & Linnartz, H. 2022, A&A, 665, A89
Radhakrishnan, S., Hager, T., Kanaherarachchi, A., et al. 2022, JCP, 157, 154201
Robert, J. S., Eric, J. M., Mark, M., et al. 2018, Proc. SPIE, 10700, 107001O
Sagan, C. 1972, Nature, 238, 77
Salpeter, E. E. 1971, Highlights Astron., 2, 429
Smith, R. S., Tylinski, M., Kimmel, G. A., & Kay, B. D. 2021, JCP, 154, 144703
Solomon, P. M., Jefferts, K. B., Penzias, A. A., & Wilson, R. W. 1971, ApJ, 168, L107
Toumi, A., Piétri, N., Chiavassa, T., & Couturier-Tamburelli, I. 2016, Icarus, 270, 435
Tschöpe, M., Schröder, B., Erfort, S., & Rauhut, G. 2021, Front. Chem., 8–2020, https://doi.org/10.3389/fchem.2020.623641
van Dishoeck, E. F., Tychoniec, Ł., Rocha, W. R. M., et al. 2025, A&A, 699, A361
Wentrup, C., Bégué, D., & Leung-Toung, R. 2017, ChemRxiv, https://doi.org/10.26434/chemrxiv.5373964.v1
Wu, Q. T., Anderson, H., Watkins, A. K., et al. 2024, ACS Earth Space Chem., 8, 79

Table A.1. Values for each variable used to calculate the dosage for each parent.

Variable	CH_3CN	CH_3CH_2CN
I (nA)	30	30
m (g mol^{-1})	41.05	55.08
e (nC)	1.6 x 10^{-10}	1.6 x 10^{-10}
N_A (molec mol^{-1})	6.02 x 10^{23}	6.02 x 10^{23}
ρ (g cm^{-3})	0.78	0.7
A (cm^2)	1.04	1.04
l (cm)	5.62 x 10^{-5}	6.16 x 10^{-5}
E_{int} (eV)	5000	5000
f_{trans}	0.0003	0.0031
E_{trans} (eV)	40	42
f_{bs}	0.0451	0.0421
E_{bs} (eV)	2794	2792
D_s (eV molec^{-1} s^{-1})	1.4 x 10^{-3}	1.9 x 10^{-3}

Appendix A: Electron irradiation dosage calculation

The electron irradiation procedure of this work is well characterized in Eq. A.1, slightly altered from the equation provided by (Förstel et al. 2015) for dose:

$$D_s = \frac{lm}{eN_A\rho Al}(E_{int} - f_{trans}E_{trans} - f_{bs}E_{bs}). \quad (A.1)$$

Within this equation, variables are defined as measurable experimental parameters, known literature values, or calculated values by Monte Carlo simulations of electron interaction with our sample through Casino 2.5 (Hovington et al. 1997). The method used to obtain each variable is listed in Table A.1. For our simulations we generate 5 x 10^6 electrons with an initial energy of 5 keV. The source is set to a 16.5 degree tilt, matching our irradiation angle within the experiments. For each parent, we use a 1000 nm thick ice with a user defined density matching the literature values for each ice (0.78 g cm^{-3} for CH_3CN and 0.7 g cm^{-3} for CH_3CH_2CN). This simulation for each electron generates a position, penetration depth, and energy deposition by depth. Furthermore, it provides the fraction of electrons which are backscattered by the ice and their energies as well as the energy of each electron which fully transmits through the ice. In Table A.1 we show the values taken for each variable to calculate the reported dosages.

Appendix B: Three-layer isonitrile confirmation experiment

In this work, we were unable to quantify CH_3CH_2NC in the gas phase following electron irradiation, which we attributed to a limit of detection based on the expected formation of the product and the known rotational transition intensity. To demonstrate the detection in the gas phase a separate experiment was performed in which a third layer of parent ice was deposited and irradiated. Furthermore, the repetition rate for millimeter-wave detection was increased by focusing on the CH_3CH_2NC and ignoring other products. Figure B.1 shows our detection of the isonitrile in the gas phase as a qualitative result.

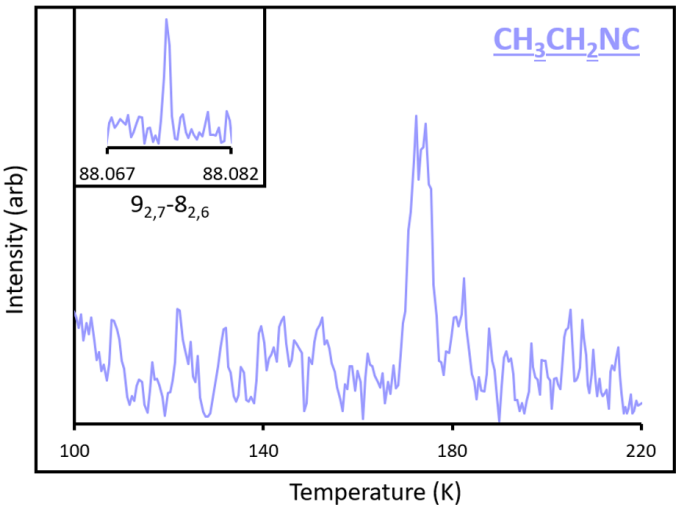

Fig. B.1. Rotational signal and TPD spectrum of CH3CH2NC from a three-layer ice experiment.